



Chapter 20

In-situ Thermal Monitoring of Printed Components During Rapid Prototyping by Fused Deposition Modeling

K. Pooladvand, A. D. Salerni, and C. Furlong

Abstract Full-field-of-view thermography is necessary to effectively monitor and control thermally driven 3D printing processes, such as Fused Deposition Modeling (FDM). The accuracy of thermographic measurements with Infrared (IR) imagers is influenced by the exact knowledge of the emissivity and absorptivity of a given material which varies depending on temperature and color. However, these material properties for ABS, one of the most widely used polymers, still need further investigation. In this paper, we present our efforts to estimate the emissivity of three differently colored ABS polymers between 40 °C and 200 °C. This range of temperatures is critical to the bond formation and welding of the polymer, which eventually defines the mechanical strength of the printed components. Using a calibrated IR imager and thermocouples, we measured the emissivity of different ABS polymeric rings at various temperatures. These measurements are based on the comparison between equivalent emissive power at measured temperatures and the measured emissions from a calibrated blackbody. This allows for the determination of subtle changes in emissivity of the ABS polymer. The estimated emissivity is mapped to correct the full-field temperature readout of the IR imager in-situ and help to accurately monitor the thermal flow. Verification was carried out based on numerical simulations to investigate several slender square blocks (e.g., 3, 7, 11 mm). The emissivity obtained by this method shows improvements in measuring accuracy. Further, our study shows that the emissivity decreases from 0.92 to 0.79 with a slower rate around the glass transition points. This 14% drop in emissivity corresponds to a difference of 36 °C at the readout temperature of 240 °C. Our results also indicate that the emissive heat flux of ABS is dependent on color. The experimentally estimated emissivity can be used in other IR cameras to correctly evaluate the temperature and monitor the thermal flow in real-time. This enables better optimization of the printing parameters to improve the bonding and strength of printed components.

Keywords 3D printing · ABS polymers emissivity · Fused deposition modeling (FDM) · IR imaging

Introduction

Applying real-time monitoring and closed-loop control to Additive Manufacturing (AM) processes can improve component performance and quality while reducing the occurrence of defects [1–4]. With this promising advancement, printing processes are actively controlled, while sensors monitor the critical parameters such as distortion, strain, pool size, heat affected zones, and temperature in-situ. The practical approaches for monitoring include optical (visual or thermal), acoustic, and contact methods [2, 5]. Optical methods offer versatile, non-contact, and full-field sensors with proper spatial and temporal resolutions to measure parameters such as temperature, shape, and distortion [5, 6]. Because 3D printing is a thermally driven process, temperature is one of the essential parameters to monitor in AM processes. Thermal energy flow and dissipation during fabrication affect the physical and mechanical properties of printed components [7–12]. Thus, thermal measurements become an indispensable tool for monitoring 3D printing technologies.

K. Pooladvand (✉) · C. Furlong

Center for Holographic Studies and Laser micro-mechaTronics – CHSLT, Worcester Polytechnic Institute, Worcester, MA, USA

Mechanical Engineering Department, Worcester Polytechnic Institute, Worcester, MA, USA

e-mail: kpooladvand@wpi.edu; cfurlong@wpi.edu

A. D. Salerni

Center for Holographic Studies and Laser micro-mechaTronics – CHSLT, Worcester Polytechnic Institute, Worcester, MA, USA

Chemical Engineering Department, Worcester Polytechnic Institute, Worcester, MA, USA

e-mail: asalerni72@wpi.edu

Thermocouples have been conventionally used for accurately measuring the temperature at specific points of interest [10, 13]. On the other hand, thermography offers full-field-of-view, non-contact, and non-invasive measurements. These superior capabilities make thermography one of the most widely used sensors in monitoring and closed-loop control systems in AM technologies [2, 3, 5, 7]. However, the thermal measurement can only measure surface temperature and is very sensitive to environmental fluctuations. Another issue is that accurate measurement requires a reliable understanding of the material properties such as emissivity and absorptivity [14–16].

Infrared (IR) cameras show promising potentials in Fused Deposition Modeling (FDM) processes. Costa et al. [12], Pooladvand and Furlong [7], and Seppala and Migler [17] have used IR cameras to estimate the material, and process properties of different 3D printed objects. In this paper, we presented our efforts to employ an IR camera in-situ to monitor the temperature in an FDM printer. We improved the accuracy of remote temperature measurements by proposing a methodology to estimate the optical properties of Acrylonitrile Butadiene Styrene (ABS) and applied it to correct imager readout in real-time.

Methodology

General Plan and Scheme of This Study

Our research combines experimental and computational approaches. In the experimental approach, the emissivity of ABS polymer was obtained empirically. We compared the responses of an IR imager from a calibrated blackbody, and ABS printed washers at different temperatures to estimate the emissivity. We curve fitted the data and used an algorithm to spatially-temporally correct temperature readouts, and map corrected temperature distribution onto specimens during manufacturing.

We also simulated a transient 1D layer-upon-layer deposition using finite difference analysis. In this simulation, boundary conditions are corrected based on the estimated convection coefficient, estimated emissivity, and the Total Heat Transfer Coefficient (THTC). The details of this numerical solution are explained here [7, 18–20]. The corrected temperature readouts were compared with our simulations. The final results illustrate how this algorithm can be used to account for the difference in emissivity and help to improve the thermal readout as a primary monitoring tool in the next generation of smart 3D printing machines.

Thermography and Infrared Camera

The radiation heat flux depends on direction, wavelength, and temperature. For most engineering materials, one can assume the directional variation is negligible in order to define heat flux in terms of wavelength and temperature, which is known as Planck's law [21, 22].

Infrared (IR) cameras are devices that receive emitted energy from an object of interest and convert them into images. The color and contrast in these images are based on the amount of energy received. The sum of the absorption, reflection, and transmission of radiative energy from each surface is equal to the total incident radiative flux. The IR cameras' detectors measure radiosity, which is a sum of reflection and emission from a particular surface. In addition, the emissivity and transitivity of the media between the source and the detector affect the temperature measurements. In theory, the total received energy contains emission from the object, reflection of other sources, losses due to transmission through and emission of the media [16]. For an object located in the atmosphere, the total energy received by the camera detector is defined as:

$$E_{tot} = \varepsilon_{obj} \cdot \tau_{atm} \cdot E_{obj} + \rho_{obj} \cdot \tau_{atm} \cdot E_{sur} + \varepsilon_{atm} \cdot E_{atm}. \quad (20.1)$$

where, E is radiation flux, τ transitivity, ρ reflectivity, and ε emissivity and subscripts tot , obj , atm , and sur denote total, object, atmosphere, and surrounding, respectively. Kirchhoff theory states for each surface the absorptivity, α , is equal to emissivity, ε , in its equilibrium condition [21, 22]. In addition, one can conclude $\rho_{obj} = 1 - \alpha_{obj}$ for opaque surfaces. The atmosphere also is a transparent medium thus, $\varepsilon_{atm} = 1 - \tau_{atm}$. Finally, the Eq. (20.1) is rewritten as:

$$E_{tot} = \varepsilon_{obj} \cdot \tau_{atm} \cdot E_{obj} + (1 - \varepsilon_{obj}) \cdot \tau_{atm} \cdot E_{sur} + (1 - \tau_{atm}) \cdot E_{atm}. \quad (20.2)$$

When the distance between detector and source is less than a meter, the effect of media can be ignored [16], and therefore τ_{atm} is equal to 1.0 and Eq. (20.2) is simplified to:

$$E_{\text{tot}} = \varepsilon_{\text{obj}} \cdot E_{\text{obj}} + (1 - \varepsilon_{\text{obj}}) \cdot E_{\text{sur}}. \quad (20.3)$$

The camera detector receives E_{tot} and uses the integrated look-up table to determine the temperature by knowing the emissivity, humidity, and distance. However, if these parameters are not defined correctly, the IR imager generally assumes the case of a blackbody object, and estimates the temperature accordingly. This process leads to an incorrect estimation of the temperature and undervalues the readouts [15, 16]. By knowing the ε , these inaccurate readouts can be corrected either during or after recording the measurements.

Thermal Modeling

Thermal flow in 3D printing has transient three-dimensional physics defined by Furrier law. However, this condition can be simplified to a one-dimensional framework assuming a lumped capacity criterion to estimate the temperature along a length of a slender cylinder or block [7, 8]. In this case, ascribing the only heat source as the advection of the newly deposited material from the extruder, the partial differential equation is obtained as:

$$\frac{\partial \rho u}{\partial t} = \frac{\partial}{\partial z} \left(\kappa \frac{\partial T}{\partial z} \right) + q_s, \quad (20.4)$$

where, t is time, u is internal energy, ρ is mass density, κ is the conductivity, T is temperature, q_s is the heat source or sink, and z is the normal to the cross-section. The heat sink is also defined as the sum of convection and radiation heat transfer ($q_s = q_{\text{conv}} + q_{\text{radi}}$). Equation 20.4 can be simplified by assuming constant area, average deposition velocity along z direction, and enthalpy formulation ($du = dh = c_p dT$):

$$\rho U c_p \frac{\partial T}{\partial z} = \kappa \left(\frac{\partial^2 T}{\partial z^2} \right) - \frac{4h_t}{d} (T - T_\infty), \quad (20.5)$$

where, U is average deposition velocity, T and T_∞ are the surfaces and environment-wall temperatures, respectively, d is a diameter or side of the cross-section, and h_t is THTC. THTC, which is found experimentally, contains both radiation and convection heat transfers. The process that led to estimating the h_t is explained in our previous work [7].

Experimental Set-up and Equipment

In our experimental measurements, we wanted to achieve three main goals: calibrating the IR camera, measuring the emissivity of three differently colored ABS polymer, and finally implementing gained knowledge to approximate the surface temperature in-situ. We designed our set up using an IR camera, type-T thermocouple, aluminum block, hot plate, calibrated blackbody, manual thermometer, aluminum tape, computer platform, high-efficiency thermal paste, and home-made cooling accessories as shown in Fig. 20.1.

The IR camera was situated above the hot plate looking to the center of the aluminum block on the hot plate (Fig. 20.1a). In addition, a home-made cooling apparatus consisting of a PVC pipe and a computer fan was utilized above the aluminum block to minimize the effects of the medium, the graphic of this configuration is shown in Fig. 20.1b. The type-T thermocouple installed between the aluminum block and the aluminum adhesive tape as shown in Fig. 20.1c, and it was connected to the DAQ using LabView to record the temperature continuously. The calibrated blackbody and the computer platform is used to determine the sensitivity of the IR camera (Fig. 20.1d).

In order to provide a stable condition, a block of aluminum with $76.03 \times 121.68 \times 37.70$ mm as shown in Fig. 20.1a, b were located on the hot plate. The top surface of the block was covered with adhesive reflective aluminum tape where the washers were positioned (Fig. 20.1c). Between the adhesive tape and aluminum block, a thermocouple was fixed and situated at the center of the block. A highly conductive thermal paste also covered the distance between the aluminum tape and the washer to guarantee the steady and constant thermal flux between two dissimilar materials and fill all the possible void areas between them.

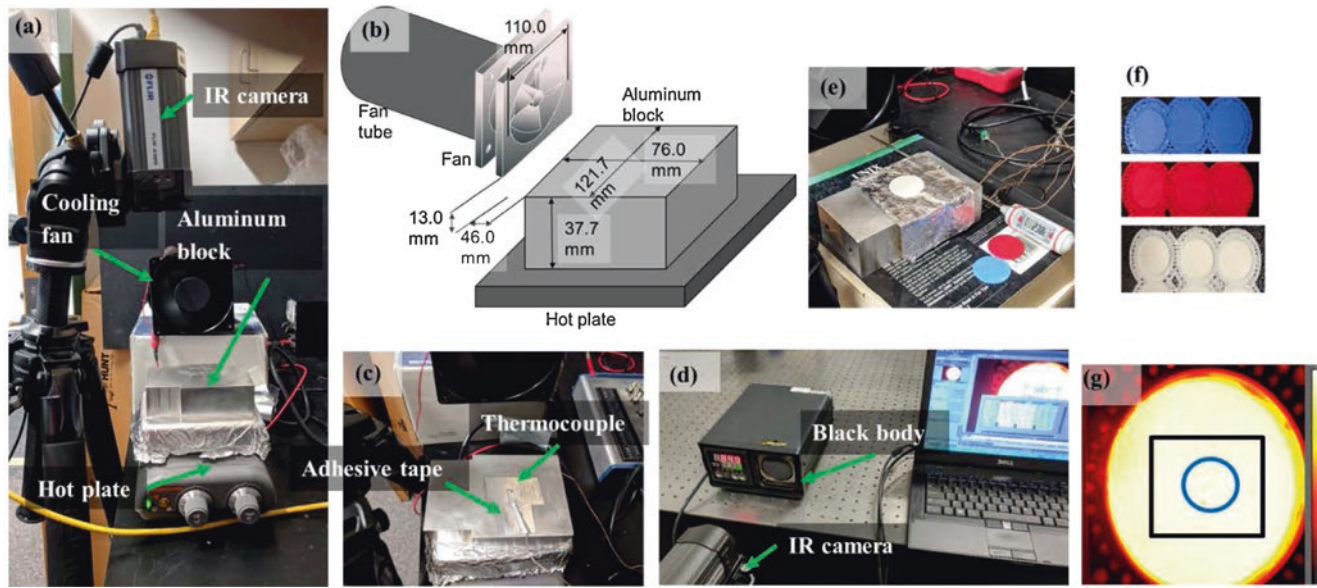


Fig. 20.1 The configuration of the setup and equipment were used for camera calibration, emissivity estimation, and temperature measurements: (a) IR camera, hot plate, and aluminum block; (b) cooling apparatus; (c) thermocouple installed between the aluminum block and the aluminum adhesive tape; (d) calibrated blackbody and the computer platform; (e) thermometer and the ABS washers; (f) the 3D printed washers consist of three sets of differently colored ABS polymers; and (g) a snapshot of the blackbody captured by the IR camera showing the Area Of Interests

Results and Discussion

IR Camera Calibration and Analysis

We used a calibrated blackbody to estimate the IR camera's response curve. Assuming the emissivity is 1.0 and the distance between the camera and the blackbody is about 200 mm, the transmissivity of the air is equal to 1.0. Therefore, the total energy received by the detector is equal to the emissive radiation from the surface of the blackbody:

$$E_{tot} = E_{obj} = E_{blackbody}. \quad (20.6)$$

We used a Microbolometer IR camera with a wide spectrum sensitivity in mid-infrared regions (7–18 μm) [20, 21], and defined the following function to represent the relationship between the camera readout and temperature, knowing that the blackbody total emissive flux follows a power function in a wide spectral range:

$$\text{readout}(T) = aT^b + c \quad (20.7)$$

The initial step was the calibration of the thermal imager under a similar environment to where the rest of the measurements were performed. Figure 20.1d shows such a setup consisted of an IR camera, computer platform, and calibrated blackbody. The temperature of the blackbody changed from 45 to 345 $^{\circ}\text{C}$ in 13 steps both ascending and descending in addition to recording room temperatures. The measurement repeated three times in the laboratory while the room temperature and humidity fluctuated between 20–25 $^{\circ}\text{C}$ and 30–45%, respectively.

At each step, the camera recorded thermograms similar to the one shown in Fig. 20.1g and the data associated with the Area Of Interests (AOI) were recorded for further analysis and curve fitting using MATLAB[®]. The curve fitting results show a strong correlation with the coefficient of determination R-square being above 0.99. Figure 20.2 shows the fitted lines and Table 20.1 lists the results of curve fitting. We did the curve fitting for three different cases, assuming the temperature in Kelvin, and degrees centigrade. Comparing the fitted curve with camera's readout in low temperature, particularly close to room temperature showed a better performance from the degree $^{\circ}\text{C}$ fitted curve.

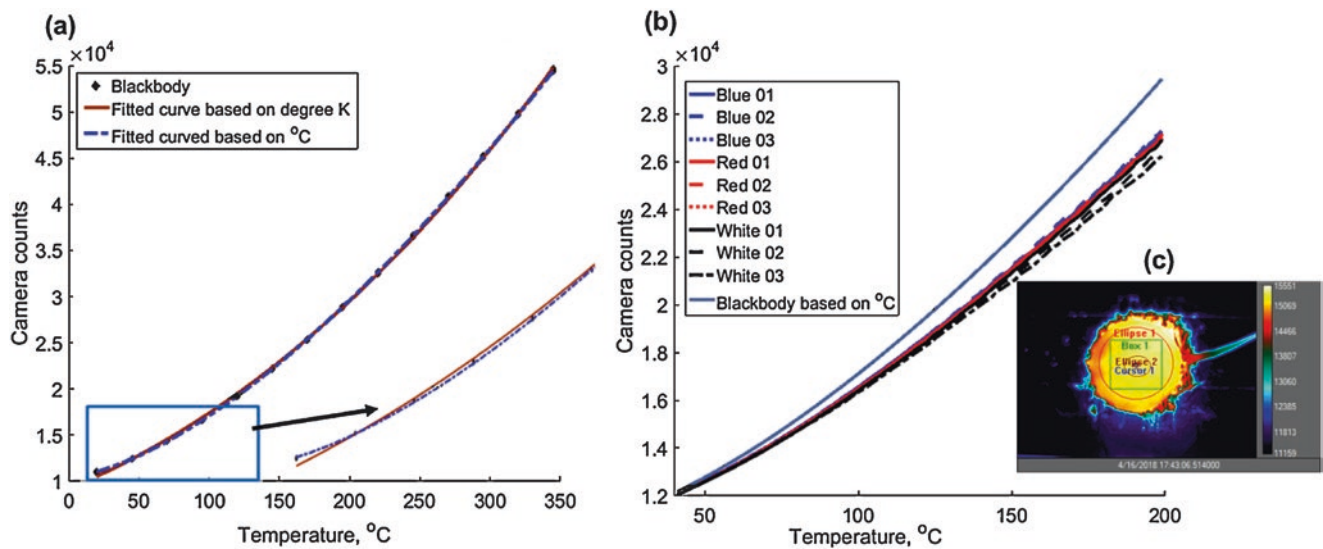


Fig. 20.2 The acquired data for blackbody and washers along with the fitted curve and snapshot of the IR camera: (a) three measurements of the blackbody with temperature ranging between 25 and 345 °C with the curved fitting based on K and °C; (b) the response curve of the blackbody juxtaposed with the nine measurements on the washers with temperatures ranging between 45 and 200 °C; and (c) a representative snapshot of the IR camera showing the different AOIs used for analyses

Table 20.1 The derived coefficient and a few statistical information of curve fitting for the rectangular and ellipsoidal AOIs used for estimating the response curves to blackbody radiation

Description	Based on Kelvin	Based on Kelvin assuming $c = 0$	Based on °C
Coefficients, a	0.008596	0.02272	5.869
Coefficients, b	2.432	2.286	1.527
Coefficients, c	1899.697	0	10464.94
R-square	0.9997	0.9998	0.9999
Root-mean-square error (RMSE)	240.0865	184.8451	61.1491

After measuring the camera's response curves, we then estimated the emissivity of the 3D printed ABS washers similar to those shown in Fig. 20.1f. We printed nine washers with a thickness of 0.8 ± 0.1 mm and a diameter of 30.0 ± 0.5 mm in three different colors and tested them with the same condition and setup. The aluminum block heated up until its top surface reached 240 °C, after which the washers were carefully situated at the center, where they made contact with the thermocouple. The thermal paste was carefully spread across the area beforehand, and a small aluminum roller was used to ensure the washers were firmly attached.

After about 5 min, the system reached a steady state, at which point the hot plate turned off and measurements started. The DAQ and the LabView® program acquired the temperatures with the data acquisition rate of 1MBs. An interface was designed to calculate the average, and standard deviation of the 10,000 subsequent acquired points and store them as a text file. In addition, the IR camera located right above the hot plate at a distance about 200 mm captured the thermograms as well. The Cold Junction (CJ) was set based on the room temperature, which was monitored continuously using a thermometer and the required changes were applied to CJ as needed. The room temperature fluctuated between 18 and 21 °C during different measurements. The humidity also monitored which was always seen as less than 40% during all measurements, though there was no significant effect on the total measurements due to the short distance between the camera and target surface.

Images and temperatures were stored and later used in Matlab for data analysis and curve fitting. The clock of the DAQ and the camera was used for matching the temporally stored data. Knowing the blackbody response at the specific temperature allowed us to measure the emissivity using Eq. (20.3) by estimating E_{obj} at the corresponding temperatures, and the IR camera's readout E_{tot} . In this equation E_{sur} was plugged in based on the room temperature measurements.

As shown in Fig. 20.2c, a few different AOIs were defined on the washer. The curve fitting and analysis were based on the data within the area of "Ellipse 2", which consisted of 732 pixels, and the comparisons among different AOIs did not show any significant differences. The total irradiances off the surface of the washers were measured in camera counts. Figure 20.2a illustrates the total readout counts of the IR camera, while Fig. 20.2b shows the fitted curves for a blackbody and three sets of measurements for white, blue, and red ABS washers. The difference between a blackbody and the ABS washers readout increases as the temperature increases, which indicates that at higher temperatures the emissivity of the ABS decreases. In general, all three different colors show relatively similar trends. Although, white ABS seems less emissive compared to that of blue and red. The difference between the latter two is negligible.

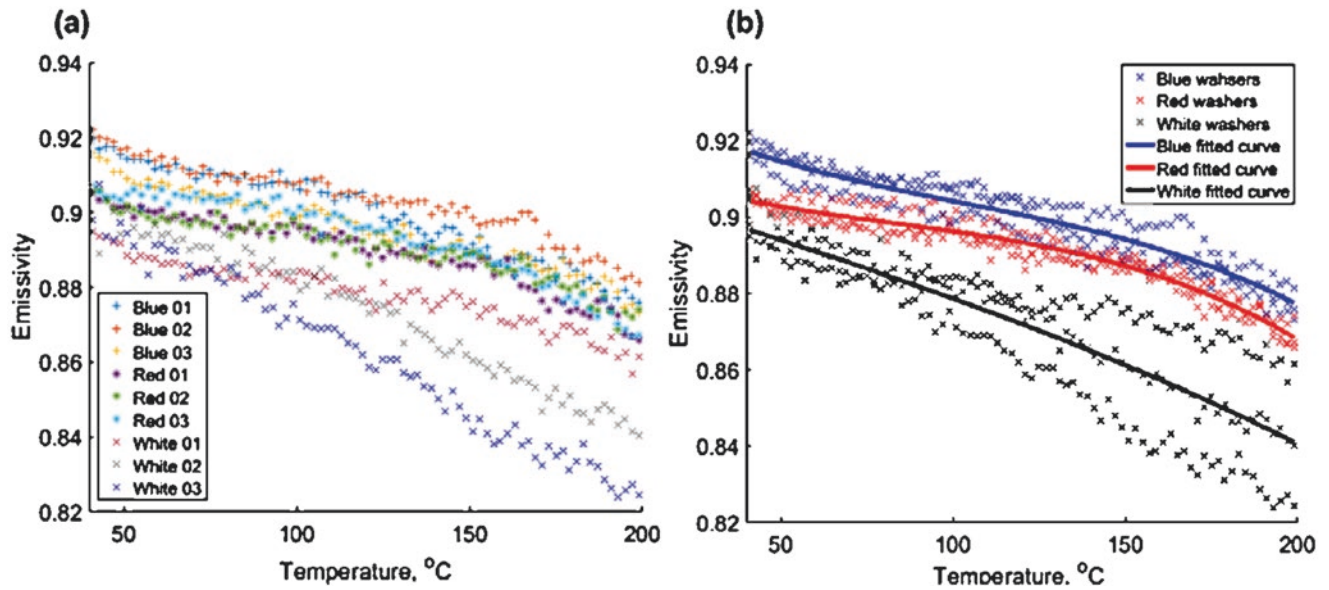


Fig. 20.3 The estimated emissivity based on the gathered data and fitted curves: (a) scatter plot shows the determined emissivity values of the nine different washers indicating a similarity in trends and effects of the colors; and (b) the entire pool of data for all measurements and the polynomial fitted curve showing the trends and the estimated values

Table 20.2 Curve fitting coefficient and a few statistical information on curve fitting for the entire obtained points for three different colored washers

Description	Blue washers	Red washers	White washers
Coefficient, a	-9.916×10^{-9}	-1.022×10^{-8}	-1.487×10^{-9}
Coefficient, b	1.118×10^{-5}	1.093×10^{-5}	1.252×10^{-6}
Coefficient, c	-0.00438	-0.004019	-0.0006367
Coefficient, d	1.497	1.405	1.019
R-square	0.8642	0.9199	0.7145
Root-mean-square error (RMSE)	0.0042	0.0028	0.100

The emissivity of these nine samples are determined and shown in Fig. 20.3a. The emissivity, in general, follows a decreasing trend as temperature increases which is similar to the behavior in other materials such as Aluminum. The maximum measured emissivity in room temperature was approximately 0.92, which is less than 0.95, the reported value for polymers at room temperature. The emissivity drops to 0.82 as temperature ascends to 200 °C for white ABS.

Figure 20.3b also illustrates all the measured points of the samples for each color, and the solid line is the fitted curve based on the entire poll of data for the same colors. A polynomial of degree 3 ($a \times x^3 + b \times x^2 + c \times x + d$) was used for the curve fitting.

Table 20.2 lists the coefficients of the polynomial along with some statistical values. The coefficient of determination is above 0.71 for white washers and above 0.86 for red and blue, which indicates a strong correlation between temperature and emissivity. These curves indicate that the difference between blue and red washers decreases as temperature increases. This data also shows that the emissivity of white washers is lower and decreases more dramatically compared to the two others. The curve fitting also exhibits a slowing slope in temperatures between 110 and 130 °C, which is attributed to the glass transition temperature of the ABS polymer.

Estimation of the Temperature Distribution Using the Estimated Emissivity in IR Camera

We printed three different ABS blocks with square cross-sections of 3, 7, and 11 mm while changing two critical printing parameters, printing speed and extruder temperature.

The first experiment was performed on a cube of 3 × 3 mm with a speed of 2000 mm/min (Low) at a temperature of 290 °C (High). The second one carried out on a cube with 7 × 7 mm, with a speed of 4000 mm/min (medium), and a temperature of 265 °C (medium), and the last cube with dimensions of 11 × 11 mm, at a speed of 6000 mm/min (High) and

a temperature of 240 °C (low). By analyzing the captured thermograms, the average deposition velocities in z -direction were calculated as 15.97, 4.66, and 2.42 mm/min for 3, 7, and 11 mm cubes, respectively. Table 20.3 indicated a few parameters along with other critical information considered for modeling.

The IR camera was installed in front of the FDM machine in a slightly inclined direction but perpendicular to the specimen at the center of the machine. The machine front door was open, and the room temperature and chamber temperature were monitored regularly. The schematic of the camera is shown in Fig. 20.4a. The printing processes were captured with a frame rate of 2 Hz from beginning to a few seconds following the completion of the specimens.

The IR camera captured the process of manufacturing three cubes printed with white ABS filament. The entire process was captured for all three cubes; however, two critical instances, halfway and completion of the printing process for the blocks of 7 and 11 mm, are demonstrated in Fig. 20.5. We wrote an algorithm to correct the IR camera's temperature measurements in-situ. The first column of images in Fig. 20.5a is the initially reported temperatures, the second column are the corrected temperatures based on emissivity, and the last column shows the temperature difference between the corrected and reported values. We used the correlation found for the white ABS polymer to account for the effect of emissivity on temperature measurements. These effects were more pronounced at higher temperatures with a maximum error of 15% in areas with temperatures above 240 °C.

Table 20.3 Part physical, geometries, and manufacturing parameters considered in this study

Length, L	30 ± 0.19 mm	Stacking orientation	Rectilinear, longitudinal (0°)
Width, w	3, 7, and 11 ± 0.5 mm	Average ideal time	0.25 s
Material	ABS	Layer thickness	0.19 mm
Color	White	Air gap	0
Specific heat, c_p	1300 J/kg-K	Average bulk temperature T_∞^a	35 °C
Density, ρ	948 ± 5 kg/cm ^{3b}	Raft	Yes
Conductivity, κ	0.16–0.15 W/m-K	Heated-bed temperature T_b	70 °C
Polymer-heated bed thermal contact coefficient	4800 W/m ² K	Bead width	0.40 mm
Coefficient of heat convection for the top layer ^c	3 mm: 90 W/m ² K 7 mm: 59 W/m ² K 11 mm: 47 W/m ² K	Linear deposition velocity for 3D	Low (2000), Medium (4000), and High (6000) (mm/min)
Coefficient of heat convection for other layers ^c	3 mm: 38 W/m ² K 7 mm: 20 W/m ² K 11 mm: 7 W/m ² K	Extruder temperature T_{Exd}	Low (240), Medium (265), and High (290) °C
Printing orientation	Vertical	Cooling	Fan speed 100%

^aThe bulk or envelope temperature was monitored using an analog thermometer and its average calculated accordingly

^bDensity was measured experimentally

^cThe correlation proposed by Churchill [23] is used to estimate the convection coefficient by assuming the velocities of 0.3 and 1.7 m/s for other and top layers, respectively

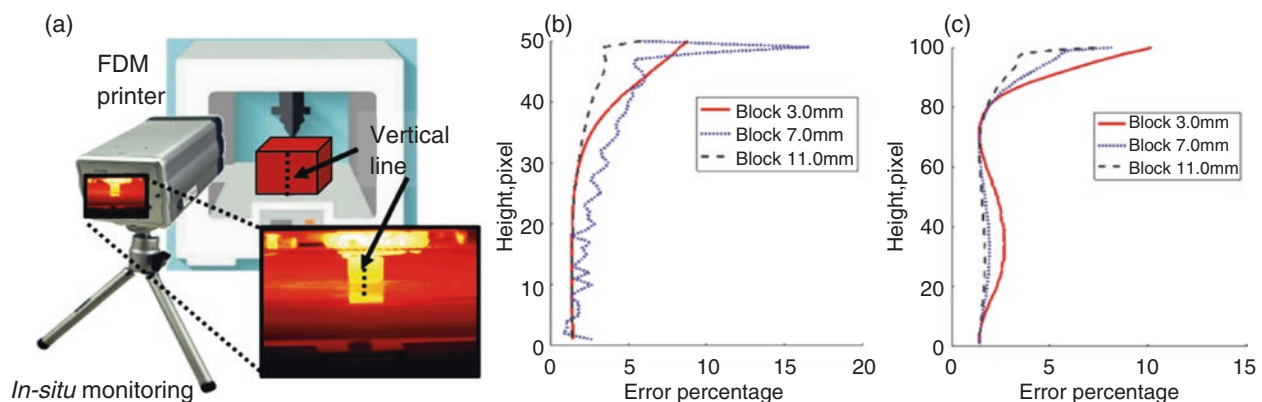


Fig. 20.4 (a) schematic of the IR camera monitoring fabrication processes in-situ; (b) Error percentage in estimation of the temperature along the height of the blocks of 3, 7, and 11 mm at the halfway point of fabrication; and (c) Error percentage in estimation of the temperature along the height of the block of 3, 7, and 11 mm upon completion of the fabrication process

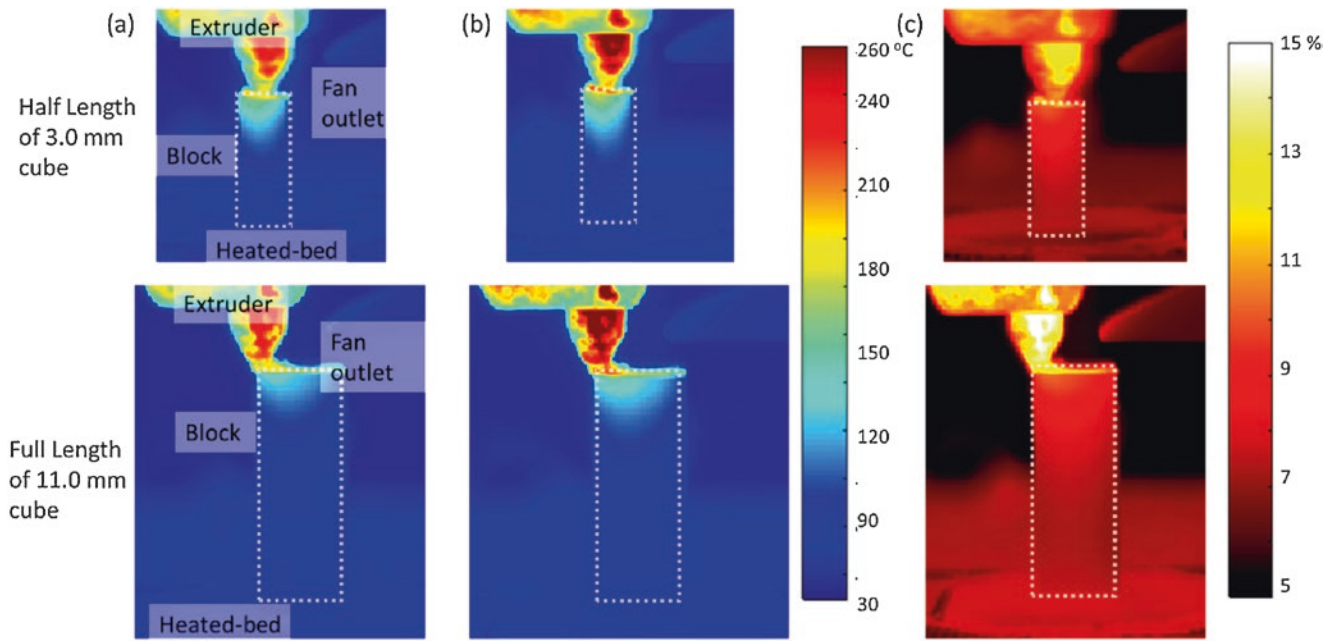


Fig. 20.5 The first and the second row show the application of the IR camera incorporating the determined emissivity for in-situ temperature measurements at half and full length specimens with 7 and 11 mm, respectively: (a) the original temperature estimated by IR camera; (b) The corrected temperature; and (c) the error percentage

Comparison Between Numerical Estimation and IR Measurements

We developed a simplified 1D simulation to estimate the temperature along the height of three different blocks with the specification mentioned in Table 20.3. The model is based on assuming the lumped capacity for the cross-sections, though this assumption only could be satisfied for the cubical section of 3×3 mm. The temperature distribution along the height of these three cases for the half and full length of the blocks are illustrated in Fig. 20.6a, b, respectively.

The results exhibit a strong agreement between the corrected temperature and the estimated temperature for each of the sizes. The maximum difference took place on the top layers of the two larger cubes. This difference can be attributed to the deficiency of a simplified 1D model to capture the dynamics of the deposition or the reflection of the extruder with a higher temperature at the top layers. The corrected temperature, except for the few top layers, are in good agreement with numerical estimation. Looking critically to the numerical model, one can conclude that the lumped capacity model as described here [24] cannot capture the correct temperature distribution and under and overestimates temperature on the lower and top layers, respectively. The temperature distribution on the areas right below the layer of the latest deposited material needs 3-dimensional analyses to be reliably estimated.

Conclusions and Future Work

In this paper, we proposed a methodology for calibration of an IR imager and estimation of the emissivity of ABS polymer using experimental data. The emissivity decreases with increasing temperature and the rates vary around the glass transition temperature of the ABS polymer. The measured emissivity shows the optical properties of ABS also depend on color with darker shades exhibiting a higher emissivity. The emissivity at room temperature is 0.92 which is below the recommended value of 0.95 of ABS commonly used in IR imagers. A script written in Matlab included the camera calibration and obtained emissivities and was incorporated into the IR imager software to correct the temperature measurement in real-time. The results exhibit up to a 15% error in temperatures measurements in temperatures as high as 240 °C which translates to 36 °C difference between uncorrected and corrected values.

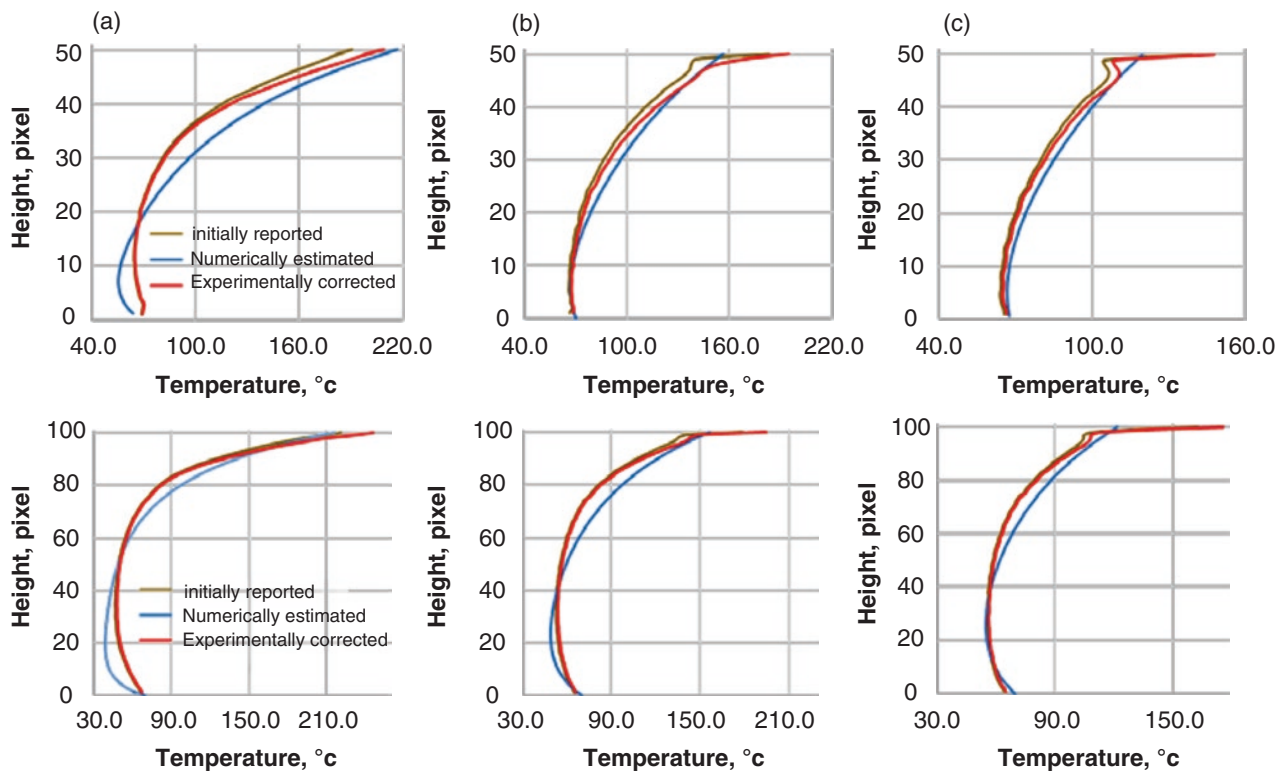


Fig. 20.6 The comparison between 1D numerical simulations, original, and corrected experimentally measured temperature along the vertical line on the center front-face for the three blocks of sizes 3, 7, and 11 mm at half and full length: (a) 3 mm cube; (b) 7 mm cube; and (c) 11 mm cube

1-D numerical simulations also verified the estimated temperatures, and the results suggest that the corrected temperatures are reliable. The estimated emissivity can be incorporated into other IR imagers monitoring ABS 3D printing processes to account for the dependency on optical material properties for accurate temperature measurements. These corrections help to improve the remote temperature measurements and can be incorporated into future FDM technologies to enable accurate thermal measurements for closed-loop control strategies.

Our results also indicate that the knowledge of the material optical properties is essential for accurate temperature measurements, and failure to incorporate this data leads to erroneous measurements which predict temperatures lower than actual values.

This study exhibits the potential of calibration and numerical modeling in the estimation of accurate thermal measurements during printing which in turn can contribute to the development of a better and more reliable 3D printer in the near future. Although, more investigation is still required to demonstrate the validity of the assumptions made, and the extension of this approach for other polymeric material and metallic 3D printers.

Acknowledgments This work has been partially supported by the NSF, award CMMI1428921. The authors would like to gratefully acknowledge the support of the Mechanical Engineering Department of Worcester Polytechnic Institute (WPI) and the contributions by members of the CHSLT.

References

1. K.D. Migler, R.E. Ricker, Measurement Science Roadmap for Polymer-Based Additive Manufacturing, (*No. Advanced Manufacturing Series (NIST AMS)-100-5*) (2016). <https://www.nist.gov/publications/measurement-science-roadmap-polymer-based-additive-manufacturing>
2. S.K. Everton, M. Hirsch, P. Stravroulakis, R.K. Leach, A.T. Clare, Review of in-situ process monitoring and in-situ metrology for metal additive manufacturing. *Mater. Des.* **95**, 431–445 (2016)
3. R.B. Dinwiddie, L.J. Love, J.C. Rowe, Real-time process monitoring and temperature mapping of a 3D polymer printing process, in *SPIE defense, security, and sensing* (International Society for Optics and Photonics, Bellingham, 2013), p. 87050L
4. C. Kousiatza, D. Karalekas, In-situ monitoring of strain and temperature distributions during fused deposition modeling process. *Mater. Des.* **97**, 400–406 (2016)
5. T. Purtonen, A. Kalliosaari, A.J.P.P. Salminen, Monitoring and adaptive control of laser processes. *Phys. Procedia* **56**, 1218–1231 (2014)
6. K. Pooladvand, C. Furlong, Digital holography and digital image correlation in additive manufacturing, in *ISEM 2015, 5th International Symposium on Experimental Mechanics* (ASEM, Guanajuato, 2015)
7. K. Pooladvand, C. Furlong, Thermo-mechanical investigation of fused deposition modeling by computational and experimental methods, in *Mechanics of Composite and Multi-Functional Materials*, vol. 7 (Springer, Cham, 2017), pp. 45–54
8. K. Pooladvand, C. Furlong, Computational and experimental characterization of 3D printed components by fused deposition modeling, in *Mechanics of Additive and Advanced Manufacturing*, vol. 8 (Springer, Cham, 2019), pp. 87–95
9. N. Shamsaei, A. Yadollahi, L. Bian, S.M. Thompson, An overview of direct laser deposition for additive manufacturing; part II: Mechanical behavior, process parameter optimization and control. *Addit. Manuf.* **8**, 12–35 (2015)
10. Q. Sun, G. Rizvi, C. Bellehumeur, P. Gu, Effect of processing conditions on the bonding quality of FDM polymer filaments. *Rapid Prototyp. J.* **14**(2), 72–80 (2008)
11. M. Griffith, M. Schlienger, L. Harwell, M. Oliver, M. Baldwin, M. Ensz, M. Essien, J. Brooks, C. Robino, e.J. Smugeresky, Understanding thermal behavior in the LENS process. *Mater. Des.* **20**(2), 107–113 (1999)
12. S.F. Costa, F.M. Duarte, J.A. Covas, Estimation of filament temperature and adhesion development in fused deposition techniques. *J. Mater. Process. Technol.* **245**, 167–179 (2017)
13. M.D. Monzón, I. Gibson, A.N. Benítez, L. Lorenzo, P.M. Hernández, M.D. Marrero, Process and material behavior modeling for a new design of micro-additive fused deposition. *Int. J. Adv. Manuf. Technol.* **67**(9–12), 2717–2726 (2013)
14. H. Krauss, C. Eschey, M. Zaeh, Thermography for monitoring the selective laser melting process. In *Proceedings of the Solid Freeform Fabrication Symposium* 999–1014 (2012). <https://sffsymposium.engr.utexas.edu/Manuscripts/2012/2012-76-Krauss.pdf>
15. E. Faye, O. Dangles, S. Pincebourde, Distance makes the difference in thermography for ecological studies. *J. Therm. Biol.* **56**, 1–9 (2016)
16. FLIR, *The Ultimate Infrared Handbook for R&D Professionals* (FLIR Systems Inc., Boston, 2012). www.FLIR.com • 1 866.477.3687, ©2012
17. J.E. Seppala, K.D. Migler, Infrared thermography of welding zones produced by polymer extrusion additive manufacturing. *Addit. Manuf.* **12**, 71–76 (2016)
18. M. Atif Yardimci, S. Güçeri, Conceptual framework for the thermal process modelling of fused deposition. *Rapid Prototyp. J.* **2**(2), 26–31 (1996)
19. L. Li, Q. Sun, C. Bellehumeur, P. Gu, Investigation of bond formation in FDM process. *Solid Freeform Fabr. Proc.* **403**, 400407 (2002)
20. L. Li, Q. Sun, C. Bellehumeur, P. Gu, Composite modeling and analysis for fabrication of FDM prototypes with locally controlled properties. *J. Manuf. Process.* **4**(2), 129–141 (2002)
21. H.R.N. Jones, *Radiation Heat Transfer* (Oxford University Press, Oxford, 2000)
22. J.R. Howell, R. Siegel, M.P. Mengüç, *Thermal Radiation Heat Transfer* (CRC Press, Boca Raton, 2011)
23. S.W.J.A.J. Churchill, A comprehensive correlating equation for forced convection from flat plates. *AIChE J.* **22**(2), 264–268 (1976)
24. C. Bellehumeur, L. Li, Q. Sun, P. Gu, Modeling of bond formation between polymer filaments in the fused deposition modeling process. *J. Manuf. Process.* **6**(2), 170–178 (2004)